Adv. Mater. **2017**, 1605837
DOI: 10.1002/adma.201605837
Article type: Communication

Modulation-Doped In_2O_3/ZnO Heterojunction Transistors processed from Solution

Dongyoon Khim, Yen-Hung Lin, Sungho Nam, Hendrik Faber, Kornelius Tetzner, Ruipeng Li, Qiang Zhang, Jun Li, Xixiang Zhang, Thomas D. Anthopoulos**

Dr. D. Khim, Dr. Y.-H. Lin, Dr. S. Nam, Dr. H. Faber, Dr. K. Tetzner, Prof. T. D. Anthopoulos
Department of Physics and Centre for Plastic Electronics, Imperial College London, South Kensington, London SW7 2AZ, UK
*E-mail: d.khim@imperial.ac.uk; thomas.anthopoulos@kaust.edu.sa

Dr. R. Li
Cornell High Energy Synchrotron Source, Wilson Laboratory Cornell University, Ithaca NY, 14853, USA

Mr. Q. Zhang, Dr. J. Li, Prof. X. Zhang
King Abdullah University of Science & Technology (KAUST), Materials Science & Engineering, Thuwal 23955-6900, Kingdom of Saudi Arabia

Prof. T. D. Anthopoulos
Division of Physical Science and Engineering
King Abdullah University of Science & Technology (KAUST)
Thuwal 23955-6900, Kingdom of Saudi Arabia

Keywords: Metal oxides; semiconductors; thin film transistors; modulation doping; heterojunction transistor; solution processing; electron mobility

Precise control of the doping level in semiconductors is essential for tuning the electronic properties and for their successful application in modern-day electronics.[1,2,3,4] Unfortunately, application of traditional doping techniques to emerging classes of semiconductors such as solution processable materials, has so far proven challenging.[5,6,7,8,9] Among a wide range of newly developed materials, metal oxides are particularly intriguing primarily due to their excellent electrical properties, optical transparency, mechanical flexibility and processing versatility.[10,11,12,13,14,15,16] Despite their tremendous potential, however, the vast majority of metal oxides are characterised by inherent stoichiometric defects which often result to

unintentional *n*-type doping.[17] Although our understanding and ability to control such defects in vacuum-grown systems has been advancing, in the case of solution-processed metal oxides it remains challenging primarily due to the multi-component nature of the precursor formulations used.[14,18,19] One approach that has often been used to circumvent this problem relies on the introduction of foreign dopant atoms.[5,9,20,21,22] In its simplest form, doping involves the physical blending of the host semiconductor with a soluble dopant agent.[5,23,24] Although attractive, the latter approach often results to dopant segregation and lattice distortions with adverse effects on charge carrier transport.

In the case of a handful of inorganic semiconductors, such negative effects can be circumvented through the use of modulation doping (MOD); a concept originally developed to negate the effect of Coulombic scattering due to the presence of ionized dopant atoms.[25,26,27,28] MOD relies on the use of an intrinsic and a doped semiconductor with different energy levels. When brought together, charge carriers flow from the doped material to the other and Fermi energy alignment occurs, causing the band edges to bend at the interface.[25,26,27,28] Under appropriate conditions, the transferred charges (holes or electrons) become confined near the interface forming a 2-dmensional electron/hole gas (2DEG/2DHG). Because of the physical separation of the space charge from the dopant atoms, carrier scattering is minimized leading to field-effect carrier mobility values close to the theoretical limit set by phonon scattering in the absence of impurity scattering.[25,26,27,28,29] Unfortunately, MOD is only applicable to semiconducting heterointerfaces of extremely high structural quality that can only be grown via sophisticated, and hence costly, techniques.[30,31]

We have recently shown that low-dimensional heterointerfaces and superlattices comprised of alternating layers of In_2O_3, ZnO or In_2O_3, Ga_2O_3, ZnO can be grown from solution at modest temperatures.[32] It the case of In_2O_3/ZnO bilayers it has been proposed that band bending occurs at the heterointerface due to electron migration from ZnO to In_2O_3 driven by the

conduction bands offsets[29,32] with the formed space charge closely resembling 2DEGs in III-V semiconductors.[33] Importantly, when the In_2O_3/ZnO heterojunctions were used as the transistor channels, a significant increase in the electron mobility and a dramatic change in the charge transport mechanism, were observed.[32] Despite the intriguing preliminary results, however, the microstructural and electronic properties of these solution-grown In_2O_3/ZnO heterojunctions have yet to be investigated.

Herein, we report the controlled growth of atomically sharp In_2O_3/ZnO and In_2O_3/Li-doped ZnO (In_2O_3/Li-ZnO) heterojunctions via spin-coating at ≤200 °C and assess their application in *n*-channel TFTs. We show that addition of Li in ZnO leads to *n*-type doping and allows for the accurate tuning of its Fermi energy (E_F). In the case of In_2O_3/ZnO heterojunctions, presence of the *n*-doped ZnO layer results to an increased amount of electrons being transferred from its conduction band minimum (CBM) to that of In_2O_3 over the interface, in a process similar to MOD. Electrical characterisation reveals the profound impact of the presence of the *n*-doped ZnO layer on the charge transport properties of the isotype In_2O_3/Li-ZnO heterojunctions as well as on the operating characteristics of the resulting TFTs. By judicious optimisation of the In_2O_3/Li-ZnO interface microstructure, and Li concentration, we demonstrate significant enhancement in both the electron mobility and TFT bias stability.

Figure 1a shows the evolution of E_F in the ZnO layer [$E_{F(Zn)}$] as a function of Li concentration measured by Kelvin Probe (KP). The E_F for the pristine In_2O_3 layer [$E_{F(In)}$= -4.57 eV] is also shown for comparison. Evidently, $E_{F(Zn)}$ depends on Li concentration and shifts by up to 0.38 eV from -4.37 eV for the pristine ZnO, to -3.99 eV for 20 wt% Li-doped ZnO [Li-ZnO (20%)]. The latter is attributed to the significant increase in the electron concentration in ZnO.[34,35] **Figure 1b** displays a diagrammatic representation of the measured $E_{F(Zn)}$ shift to higher energies with increasing Li concentration in relation to $E_{F(In)}$, while **Figure 1c** shows the resulting change in the difference between $E_{F(Zn)}$ and $E_{F(In)}$ denoted as ΔE_F. Larger values

for ΔE_F are expected to increase the amount of electrons being transferred from the CBM of ZnO to that of In_2O_3 upon contact, leading to a significant increase in the interface's conductivity in a similar manner to MOD III-V heterostructures.[36]

To verify, or indeed refute this hypothesis, we measured the sheet resistance (R_{SH}) for the single ZnO and In_2O_3 layers as well as for the In_2O_3/ZnO and In_2O_3/Li-ZnO(2-20%) heterojunctions. Pristine ZnO and In_2O_3 layers are known to exhibit a wide range of R_{SH} values (10^4-10^{-4} Ω/□), primarily due to stoichiometric differences and sample geometries.[22,37] Since both the In_2O_3 and ZnO layers studied here were extremely thin (<10 nm), the R_{SH} values for both pristine and Li-doped systems were found to be very high (>100 MΩ/□) and well beyond our measurement range. Isotype In_2O_3/ZnO heterojunctions, on the other hand, exhibited significantly lower R_{SH} with a strong dependence on Li concentration. **Figure 1d** displays the evolution of R_{SH} for In_2O_3/Li-ZnO heterojunctions as a function of Li concentration (%) measured using the four-point probe technique (**Figure 1d**, inset). The large drop in R_{SH} seen with increasing Li concentration indicates an increase in the heterojunction conductance suggesting effective MOD.

The surface topographies of the studied pristine and Li-doped ZnO and In_2O_3/ZnO were examined using atomic force microscopy (AFM). Representative AFM images are shown in **Figures 2a**-**2b** as well as in **Figure S1**. In both single layers and heterojunctions, the surface of the undoped ZnO layer appears continuous with no significant differences between the surface topographies. Upon Li incorporation, however, ZnO becomes smoother for Li concentrations up to 5 wt% followed by a moderate increase at >10 wt%. This effect is better illustrated in **Figure 2c** where the evolution of the root means square of the surface roughness (R_{RMS}) extracted from the AFM images for each sample is plotted as a function of Li concentration. Evidently, the In_2O_3/Li-ZnO(5%) heterojunction exhibit the flattest surface with R_{RMS} = 0.36 nm.

The quality of the In_2O_3/Li-ZnO heterointerface was further examined using x-ray reflectivity (XRR) measurements [**Figure 2d** (solid lines)]. All heterojunctions could be modelled as simple bilayers [**Figure 2d** (dashed lines)], allowing calculation of the surface (ZnO/Air) and heterointerface (In_2O_3/ZnO) roughness. We note, however, that the R_{RMS} values extracted are approximate since deviations between the experimental data and theoretical fittings exist, a feature indicating the presence of a non-ideal heterointerface. The R_{RMS} value of the top ZnO/Air interface is found to decrease with increasing Li wt%, in agreement with the AFM data, also shown in **Figure 2c**. Interestingly, the In_2O_3/ZnO interface appears ultra-smooth with R_{RMS} value in the range 0.18-0.23 nm, which is smaller than that for SiO_2 (0.27-0.28 nm), demonstrating the superior quality of the In_2O_3 layer. The layer thicknesses for In_2O_3 and ZnO were also calculated from the XRR fittings in **Figure 2d** (dashed lines) yielding values in the ranges of 3-4 nm and 6-7 nm, respectively.

To gain more insight into the impact of Li doping on the microstructure of ZnO, we conducted grazing incidence x-ray diffraction (GID) measurements on pristine and *n*-doped (5-20 wt% Li concentrations) single ZnO layers (**Figure 2e**). All samples showed powder-like diffraction patterns with a typical ZnO Wurtzite crystal structure. The similarity in the diffraction peaks indicates that the ZnO microstructure is preserved following Li incorporation, possibly suggesting an interstitial rather than a substitutional doping process. However, further work is required to elucidate the exact mechanism.

The microstructure of the In_2O_3/ZnO heterojunction was further examined by cross-sectional high-resolution transmission electron microscopy (HRTEM). **Figure 3a** shows the cross-sectional HRTEM image of an isotype In_2O_3/ZnO heterojunction grown on Si^{++}/SiO_2. The HRTEM data provide the first direct evidence of the existence of two discrete polycrystalline layers separated by an atomically sharp heterointerface. Analysis of the bottom In_2O_3 layer in the image reveal a lattice spacing of 0.29 nm corresponding to the (222) plane, while for the

top ZnO layer two prominent lattice spacings of 0.26 nm [(002) plane] and 0.28 nm [(100) plane], were identified. Interestingly, addition of Li up to 20 wt% concentrations in the precursor solution of ZnO does not appear to have a noticeable impact on the layer microstructure, in agreement with the XRD results (**Figure 2e**). Finally, analysis of the HRTEM image yields layer thicknesses for In_2O_3 and for ZnO in the range of 3-5 nm, and 6-7 nm, respectively, in good agreement with the XRR data in **Figure 2d**.

The elemental composition of the In_2O_3/ZnO heterojunction was also studied using scanning transmission electron microscopy (STEM) and electron energy loss spectroscopy (EELS). The top image in **Figure 3b** displays a STEM image of the heterojunction, whilst the image below show the elemental maps for Zn and In for the same cross-section. In agreement with the XRR and HRTEM analysis, the EELS results confirm the existence of discrete ultrathin layers of In_2O_3 and ZnO layers separated by a chemically sharp heterointerface. Interestingly, weak signatures of Li atoms could only be detected in In_2O_3/Li-ZnO(20%) heterojunctions (**Figure S2**), possibly suggesting an extremely low concentration of Li in the solid ZnO layer. However, accurate quantification of the Li content would require further work using complementary analytical techniques.

To investigate the charge transport properties of the pristine In_2O_3/ZnO and *n*-type doped In_2O_3/Li-ZnO heterojunctions, we fabricated a series of bottom-gate, top-contact (BG/TC) transistors. Prior to this, however, the effect of Li incorporation on the electrical properties of single layer-based ZnO and In_2O_3 devices, was investigated. **Figures S3a** and **S3b** show the transfer characteristics and electron mobility (μ_{SAT}), measured in saturation, for ZnO and Li-ZnO TFTs. Pristine ZnO devices exhibit μ_{SAT} = 1.51 (±0.3) $cm^2V^{-1}s^{-1}$ with onset voltage (V_{ON}) of -19 V, both consistent with previously published results.[31] Li-ZnO TFTs show enhanced μ_{SAT} values of up to 2.34 (±0.42) $cm^2V^{-1}s^{-1}$ for Li concentrations up to 5%, followed by a monotonic decrease at higher Li concentrations (**Figure S3b**). A similar trend is observed in

the V_{ON} which is found to shift towards negative gate voltages (V_G) for Li concentrations ≤5 wt%, indicating a higher concentration of free electrons, followed by a return to more positive V_G for Li concentrations >5 wt%. The latter is attributed to trap formation due to the suppressed ZnO crystallinity and/or Coulomb scattering.[1,38] Contrariwise to ZnO devices, electron transport in In_2O_3 TFTs deteriorated upon Li incorporation (**Figure S4**). Based on these data, we conclude that Li *n*-type doping is only applicable to ZnO.

To examine the impact that Li *n*-type doping of ZnO layer has on the electrical properties of In_2O_3/ZnO TFTs, we fabricated a series of devices in which the Li concentration was varied between 0-30 wt%. **Figure 4a** shows the transfer and $I_D^{0.5}$ vs. V_G characteristics for various In_2O_3/Li-ZnO(0-30%) TFTs, whilst the key transistor parameters are summarized in **Figure 4b** and **Table 1**. Pristine In_2O_3/ZnO TFTs show good *n*-channel operation with negligible hysteresis, high current on/off ratio of $>10^5$ and μ_{SAT} = 3.2 (±0.3) $cm^2V^{-1}s^{-1}$. The latter value is higher than μ_{SAT} obtained for single layer In_2O_3 and ZnO TFTs, and is certainly partly responsible for the reduced R_{SH} observed in **Figure 1d**. Clearly, Li incorporation leads to dramatic changes in the operating characteristics of all heterojunction TFTs, the magnitude of which depends on the initial Li concentration employed. The effect of the increased μ_{SAT} is better illustrated in **Figure 4b**, where the "on current" of the pristine In_2O_3/ZnO TFTs is seen to increase from 5.2×10^{-4} A, to 1.2×10^{-2} A for the In_2O_3/Li-ZnO(30%) device. The linear dependence of V_{ON} on Li concentration, which reduces from -10 V for Li = 0 wt%, to -50 V for Li = 30 wt%, is also indicative of the increased number of free electrons transferred from the CBM of ZnO to that of In_2O_3 driven by the increased ΔE_F (**Figure 1b-c**). The improved μ_{SAT} and enhanced free electron concentration in the channel are in agreement with the R_{SH} trend shown in **Figure 1d**.

Assuming that the transferred electrons are confined at the In_2O_3/ZnO heterointerface (a good approximation considering the low dimensional nature of the heterojunction) one can

estimate the increase in the electron areal/volume density ($\Delta n_e/\Delta n_{3D}$) within the channel due to extrinsic *n*-doping using $\Delta n_e = (\Delta V_{ON} \times C_i/q)$, where ΔV_{ON} represents the shift of channel switch-on voltage upon Li-doping at each concentration, C_i is the capacitance of the gate dielectric normalized to the channel area, and q the elementary charge. The value of Δn_{3D} was estimated by dividing Δn_e with the volume of the semiconductor layer assuming an average In_2O_3 thickness of 4.5 nm and a uniform electron distribution across the layer. **Figure 4c** shows the evolution of Δn_e and Δn_{3D} with Li concentration. The linear increase of $\Delta n_e/\Delta n_{3D}$ to 2.2×10^{12} cm^{-2} / 4.8×10^{18} cm^{-3} for 20 wt% Li concentration, is consistent with the MOD process and is responsible for the "semiconductor-to-metal" like transition observed in **Figure 4a** (Li = 30 wt% curve) as well as for the sharp drop of R_{SH} in **Figure 1d**.

Another important characteristic associated with the In_2O_3/Li-ZnO TFTs is the enhanced μ_{SAT} observed across all Li concentrations. As shown in **Figure 4d**, μ_{SAT} increases continuously with increasing Li concentration up to a maximum value of 11.4 (±1.7) $cm^2V^{-1}s^{-1}$ for 10 wt% beyond which it remains constant. This is not the case for single layer In_2O_3 TFTs, where μ_{SAT} reduces upon Li introduction. The later observation may well be related to adverse effects that Li incorporation may have on the microstructure of In_2O_3. To this end, Pramod *et al*., recently reported that Li doping of In_2O_3 reduces its average crystallite size, leading to an increase in the layer resistivity and optical band gap [39]. Unfortunately, the extremely thin nature of the In_2O_3 layers studied here did not allowed us to verify whether such structural changes occur upon Li-doping. Interestingly, ZnO TFTs show a small increase in μ_{SAT} for Li concentrations up to 5 wt% followed by a reduction at higher doping levels. The continuous increase in $\Delta n_e/\Delta n_{3D}$ and μ_{SAT} values seen in **Figure 4c** and **Figure 4d**, respectively, for In_2O_3/ZnO TFTs indicate that in the heterojunction channel electron transport remains largely unaffected by the presence of Li atoms in the ZnO layer even at very high concentrations,

which is not the case for any of the single layer devices (**Figures S3-S4**). This characteristic resembles traditional high electron mobility transistors (HEMTs) based on AlGaAs/GaAs channels where the resulting free electrons are spatially separated from the donor ions (dopants). The latter feature leads to dramatically reduced electron scattering due to Coulombic interactions with the dopant ions leading to ultra-high mobility values.[33] Based on these results we conclude that electron transport in *n*-doped isotype In_2O_3/Li-ZnO heterojunction channels takes place within the In_2O_3 layer and as such is not limited by Coulomb scattering since the Li atoms are located in the top ZnO layer. Therefore, the role of Li-ZnO is merely to supply free electrons to the highly crystalline In_2O_3 layer without disrupting its microstructure and hence long-range transport.

A further advantage associated with the MOD In_2O_3/Li-ZnO transistors is the small mobility variation between devices. This effect is better illustrated in **Figure 4e** where the electron mobility for 28 different MOD In_2O_3/Li-ZnO(20%) transistors is plotted as a function of device number. All transistors exhibit high mobility and small device-to-device variation with an average and maximum μ_{FET} of 11.4 $cm^2V^{-1}s^{-1}$ (standard deviation of 1.69) and 16 $cm^2V^{-1}s^{-1}$, respectively. Additionally, the MOD In_2O_3/Li-ZnO(20%) TFTs show significantly improved bias stability as can be seen in **Figure S5**. Under continuous bias application of V_G = 60 V and V_D = 10 V, the channel current (I_D) in the MOD In_2O_3/Li-ZnO(20%) TFT is found to decrease by approximately 16% as compared to the significant drop of 44% observed for the pristine In_2O_3/ZnO heterojunction TFT. This significant difference is most likely ascribed to different trap distributions present at the heterointerface and/or bottom SiO_2/In_2O_3 channel interface. Although very promising, the results are preliminary and further work is required to elucidate the origin of this effect.

In conclusion, we demonstrated modulation doping of solution-processed isotype In_2O_3/ZnO heterojunctions and their application in *n*-channel TFTs. Despite the simplicity and low-

temperature nature of the growth processes employed, the resulting In_2O_3/ZnO heterojunctions exhibit long-range uniformity and a surprisingly sharp heterointerface. These attributes combined with the significant ΔE_F present between In_2O_3 and ZnO aid the formation of space charge in the vicinity of the heterojunction. Selective *n*-type doping of the top ZnO layer with Li was shown to increase the ΔE_F and as a consequence the number of free electrons transfer from ZnO to the CBM of In_2O_3. This simple but yet powerful modulation doping approach was shown to yield In_2O_3/Li-ZnO TFTs with significantly improved operating characteristics such as enhanced electron mobility and operating stability. This is the only demonstration of a MOD metal oxide TFT fabricated from solution-phase and highlights new opportunities towards design and development of novel TFT concepts.

Experimental Section

Oxide Precursor Preparation: ZnO precursor solutions were prepared by dissolving ZnO nanopowder (>97 % Sigma-Aldrich) in ammonium hydroxide (50% v/v; Alfa Aesar) at 8 $mgmL^{-1}$ and stirred at room temperature for 24 hours before using. In_2O_3 precursor solutions were prepared by dissolving anhydrous indium nitrate (In(NO3)3, 99.99%; Indium Corporation) in 2-Methoxyethanol at 20 $mgmL^{-1}$ and stirred at room temperature for 24 hours before processing. Lithium acetate ($LiOOCCH_3$) was used as the source of Li and was dissolved in a (1:1) blend of ammonium hydroxide and 2-Methoxyethanol). Li-doping of the ZnO and In_2O_3 precursor formulations was implemented via solution blending with the Lithium acetate solution at appropriate wt%.

Transistor Fabrication: Wafers composed of heavily doped silicon (Si^{++}), acting as the gate electrode, and a thermally grown SiO_2 layer (400 nm or 100 nm thick) as the gate dielectric were used as the substrates. As-received wafers were cleaned in ultra-sonic baths of deionized water, acetone, and iso-propanol, sequentially, for 10 min each. The substrates were then

subject to the UV ozone treatment in order to improve the wettability of the surfaces before spin-cast of the precursor formulations. In_2O_3 and ZnO were both deposited by spin-coating in air. In_2O_3 precursor solution was first coated onto Si^{++}/SiO_2 wafers at 4000 rpm for 30s and annealed at 200°C for 45 min. The In_2O_3 layer was then subjected to a 5-min UV ozone treatment in order to increase its surface wettability and improve the material stoichiometry. ZnO (or Li-ZnO) precursor solution was spin-coated at 6000 rpm for 30 s and annealed at 200°C for 45 min. The entire film deposition process was carried out in ambient atmosphere. In_2O_3/ZnO heterojunctions were grown through sequential deposition of the two materials using the same conditions. Transistor fabrication was completed with the deposition of the top Al (40 nm) source/drain electrodes via thermal sublimation through metal stencil masks in high vacuum (10^{-6} mbar).

Thin Film Characterization: Atomic Force Microscopy was carried out in tapping mode using an Agilent 5500 atomic force microscope in ambient atmosphere. The approximate resonance frequency of the cantilever was 250 kHz and force constant was approximately 60 Nm^{-1}. All the samples were prepared on Si^{++}/SiO_2 substrates. The UV-vis transmission measurements were performed using a Shimadzu UV-2600 UV-vis spectrophotometer. The samples were prepared on quartz substrates using the same deposition parameters described above. Fermi levels of the thin-film layers were taken using a KP Technology scanning Kelvin probe system SKP5050 in nitrogen environment at room temperature.

Grazing Incident Diffraction and X-Ray Reflectivity Measurements: Grazing incident diffraction and x-ray reflectivity were carried out on beamline G2 at Cornell High Energy Synchrotron Source (CHESS), Cornell University. The thin films samples were aligned on a Kappa diffractometer with the X-ray energy of 11.56 keV (λ = 1.073 Å) through a Be single-crystal monochromator. The data were collected using a 640-element 1D diode-array detector, with a set of 0.1° Soller slits mounted on the detector arm to provide an in-plane resolution of

0.16°. The grazing incident angle was fixed at 0.15° in GID, except noted angles. The GID data set was integrated from 0.1° to 2° on the linear detector. The x-ray reflectivity (XRR) measurements were carried out in the θ-2θ mode with the 2θ range of 0° to 4°. The fitting was performed by the program Parratt32.[40]

HETEM, EELS& EDS mapping: The samples for TEM observation were prepared by focused ion beam (FIB) processing techniques. A gold plated layer with thickness of 5 nm was coated on sample via sputter before TEM sample preparation to make its surface more conductive. The high-resolution TEM (HRTEM) images of samples were all acquired by FEI Titan G2 60-300 microscope equipped with a spherical aberration corrector for imaging system. The HRTEM images and elemental mappings (EELS mapping and EDS mapping) of samples were all acquired at 300kV by FEI Titan G2 80-300 microscope equipped with a high-brightness Schottky-field emission electron source and a high-resolution Gatan Imaging Filter (GIF) Tridiem energy-filter.

Transistor characterization: The FET electrical characterisation was carried out using an Agilent B2902A parameter analyzer in a nitrogen-filled glove box. The μ_{FET} and V_{Th} values were extracted at the saturation region using the gradual channel approximation equation.

Supporting Information

Supporting Information is available online from the Wiley Online Library or from the author.

Acknowledgements

D.K., Y.H.L., H.F., and T.D.A. are grateful to the European Research Council (ERC) AMPRO project no. 280221 for financial support. Q.Z., J.L., and X.X.Z., are grateful to KAUST for the financial support. CHESS is supported by the NSF & NIH/NIGMS via NSF award DMR-1332208.

Received: ((will be filled in by the editorial staff))
Revised: ((will be filled in by the editorial staff))
Published online: ((will be filled in by the editorial staff))

References

[1] S. M. Sze, K. K. Ng, *Physics of Semiconductor Devices, John Wiley & Sons, Inc., Hoboken, NJ, USA*, **2006**.

[2] D. M. Caughey, R. E. Thomas, *Proc. IEEE* **1967**, *55*, 2192.

[3] W. E. Spear, P. G. Lecomber, *Solid State Commun*. **1975**, *17*, 1193.

[4] P. Siffert, E. Krimmel, Silicon: Evolution and Future of a Technology, Springer-Verlag, New York, USA 2004.

[5] S. Y. Park, B. J. Kim, K. Kim, M. S. Kang, K.-H. Lim, T. I. Lee, J. M. Myoung, H. K. Baik, J. H. Cho, Y. S. Kim, *Adv. Mater*. **2012**, 24, 834.

[6] B. Lüssem, M. Riede, K. Leo, *Phys. Status Solidi A* **2013**, 210, 9.

[7] D. Khim, K.-J. Baeg, M. Caironi, C. Liu, Y. Xu, D.-Y. Kim, Y.-Y. Noh, *Adv. Funct. Mater.* **2014**, 24, 6252.

[8] B. D. Naab, S. Zhang, K. Vandewal, A. Salleo, S. Barlow, S. R. Marder, Z. Bao, *Adv. Mater*. **2014**, 26, 4268.

[9] Y.-H. Lin, S. R. Thomas, H. Faber, R. Li, M. A. McLachlan, P. A. Patsalas, T. D. Anthopoulos, *Adv. Electron. Mater*. **2016**, 2, 1600070.

[10] K. Nomura, H. Ohta, A. Takagi, T. Kamiya, M. Hirano, H. Hosono, *Nature* **2004**, 432, 488.

[11] E. M. C. Fortunato, P. M. C. Barquinha, A. C. M. B. Pimentel, A. M. F. Goncalves, A. J. S. Marques, R. F. P. Martins, L. M. N. Pereira, *Appl. Phys. Lett*. **2004**, *85*, 2541.

[12] Y.-H. Kim, J.-S. Heo, T.-H. Kim, S. Park, M.-H. Yoon, J. Kim, M. S. Oh, G.-R. Yi, Y.-Y. Noh, S. K. Park, *Nature* **2012**, *489*, 128.

[13] M.-G. Kim, M. Kanatzidis, A. Facchetti, T. Marks, *Nat. Mater*. **2011**, *10*, 382.

[14] K. K. Banger, Y. Yamashita, K. Mori, R. L. Peterson, T. Leedham, J. Rickard, H. Sirringhaus, *Nat. Mater*. **2011**, *10*, 45.

[15] E. Fortunato, P. Barquinha, R. Martins, *Adv. Mater*. **2012**, *24*, 2945.

[16] X. Yu, T. J. Marks, A. Facchetti, *Nat. Mater*. 2016, 15, 383.

[17] E. G. Seebauer, M. C. Kratzer. *Charged Semiconductor Defects: Structure, Thermodynamics and Diffusion*, Springer-Verlag, London, UK **2009**.

[18] M. Niederberger, *Acc. Chem. Res*. **2007**, *40*, 793.

[19] T. Trindade, J. D. Pedrosa de Jesus, P. O'Brien, *J. Mater. Chem*. **1994**, *4*, 1611.

[20] J. G. Lu, Y. Z. Zhang, Z. Z. Ye, Y. J. Zeng, H. P. He, L. P. Zhu, J. Y. Huang, L. Wang, J. Yuan, B. H. Zhao, X. H. Li, *Appl. Phys. Lett*. **2006**, *89*, 112113.

[21] F. K. Shan, B. I. Kim, G. X. Liu, Z. F. Liu, J. Y. Sohn, W. J. Lee, B. C. Shin, Y. S. Yu, *J. Appl. Phys*. **2004**, *95*, 4772.

[22] A. Janotti, C. G. Van de Walle, *Rep. Prog. Phys. 2009*, **72**, 126501.

[23] C. Liu, J. Jang, Y. Xu, H.-J. Kim, D. Khim, W.-T. Park, Y.-Y. Noh, J.-J. Kim, *Adv. Funct. Mater*. **2015**, *25*, 758.

[24] T. Menke, D. Ray, J. Meiss, K. Leo, M. Riede, *Appl. Phys. Lett.* **2012**, *100*, 093304.

[25] R. Dingle, H. L. Störmer, A. C. Gossard, W. Wiegmann, *Appl. Phys. Lett*. **1978**, *33*, 665.

[26] T. Ando, A. B. Fowler, F. Stern, *Rev. Mod. Phys*. **1982**, *54*, 437.

[27] T. J. Drummond, W. T. Masselink, H. Morkoc, *Proc. IEEE* **1986**, *74*, 773.

[28] D. Delagebeaudeuf, N. T. Linh, *IEEE Trans. Electron Devices* **1982**, *29*, 955.

[29] J. G. Labram, Y.-H. Lin, T. D. Anthopoulos, *Small* **2015**, *11*, 5472.

[30] A. Ohtomo, D. A. Muller, J. L Grazul, H. Y. Hwang, *Nature*, **2002**, 419, 378.

[31] A. Ohtomo, H. Y. Hwang, *Nature*, **2004**, 427, 423.

[32] Y.-H. Lin, H. Faber, J. G. Labram, E. Stratakis, L. Sygellou, E. Kymakis, N. A. Hastas, R. Li , K. Zhao, A. Amassian, N. D. Treat, M. McLachlan, T. D. Anthopoulos, *Adv. Sci.* **2015**, *2*, 1500058.

[33] T. J. Drummond, W. R. Masselink, H. Morkoc, *Proc. IEEE* **1986**, *74*, 773.

[34] P. Li, S.H. Deng, Y.B. Li, J. Huang, G.H. Liu, L. Zhang, *Physica B*, **2011**, *406*, 3125.

[35] M. J. Akhta, H. A. Alhadlaq, A. Alshamsan, M. A. Majeed Khan, M. Ahamed M, *Sci. Rep*. **2015**, *5*, 13876.

[36] H. L. Störmer, A. C. Gossard, W. Wiegmann, K. Baldwin, *Appl. Phys. Lett*. **1981**, *39*, 912.

[37] K. Ellmer, *J. Phys. D: Appl. Phys*. **2001**, *34*, 3097.

[38] D. Chattopadhyay, H. Queisser, *Rev. Mod. Phys*. **1981**, *53*, 745.

[39] N. G. Pramod, and S. N. Pandey, *Ceramics International* **2015**, *41*, 527.

[40] C. Braun, *Parratt32. Version 1.5. HMI*, Berlin, Germany, **1997**.

Figures and Tables

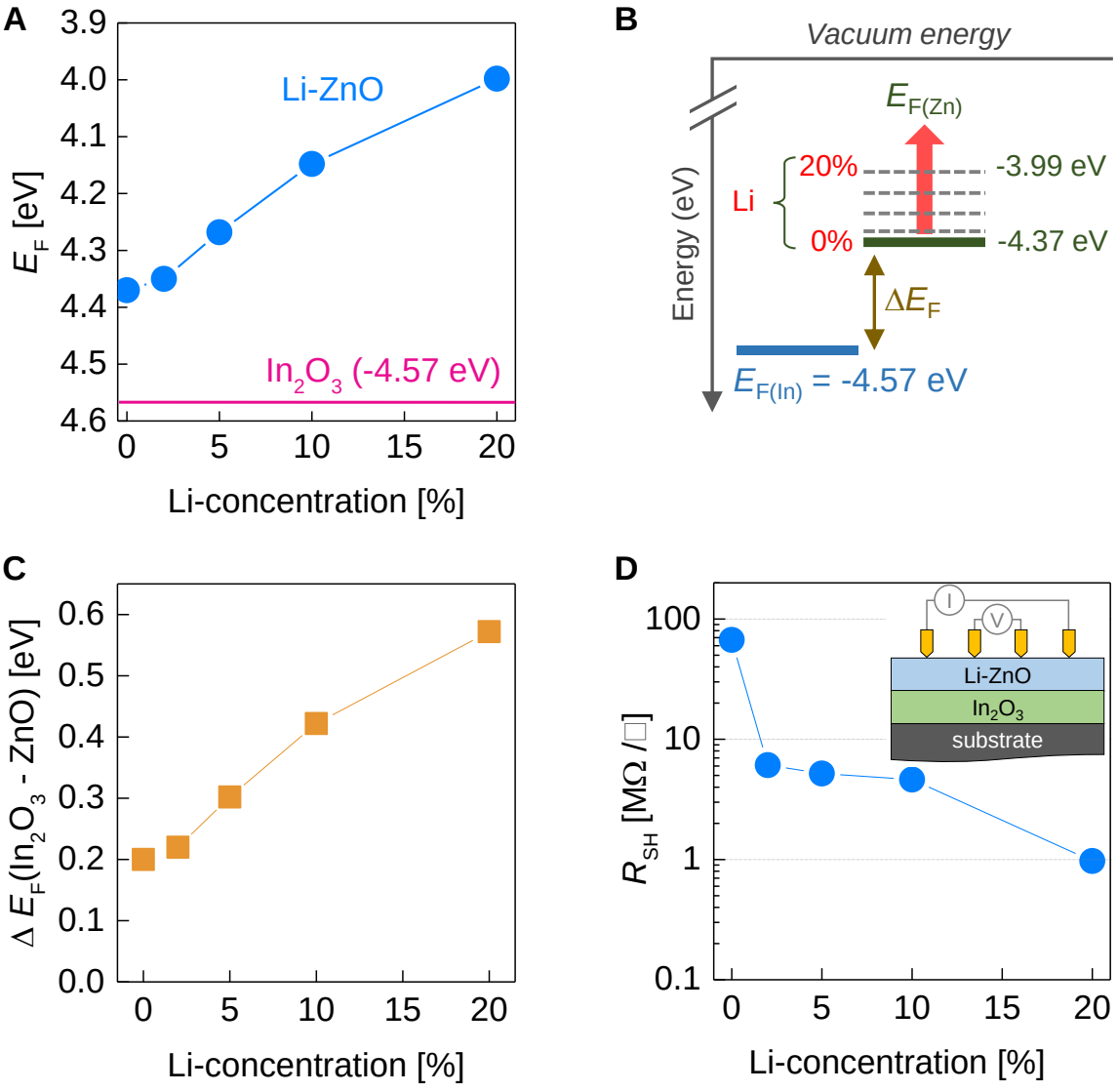


Figure 1. (a) Evolution of the Fermi energy level in In_2O_3 and ZnO layers as a function of Li concentration measured by Kelvin probe (KP). (b) Schematic energy band diagram illustrating the shift of $E_{F(Zn)}$ to higher energies with increasing Li concentration in relation to $E_{F(In)}$. (c) Dependence of the difference between $E_{F(Zn)}$ and $E_{F(In)}$ (denoted as ΔE_F) as a function of Li concentration. (d) Sheet resistance measured for the In_2O_3/ZnO heterojunctions before and after n-type doping of the top ZnO layer with Li at different concentrations measured using the 4-point probe method (inset).

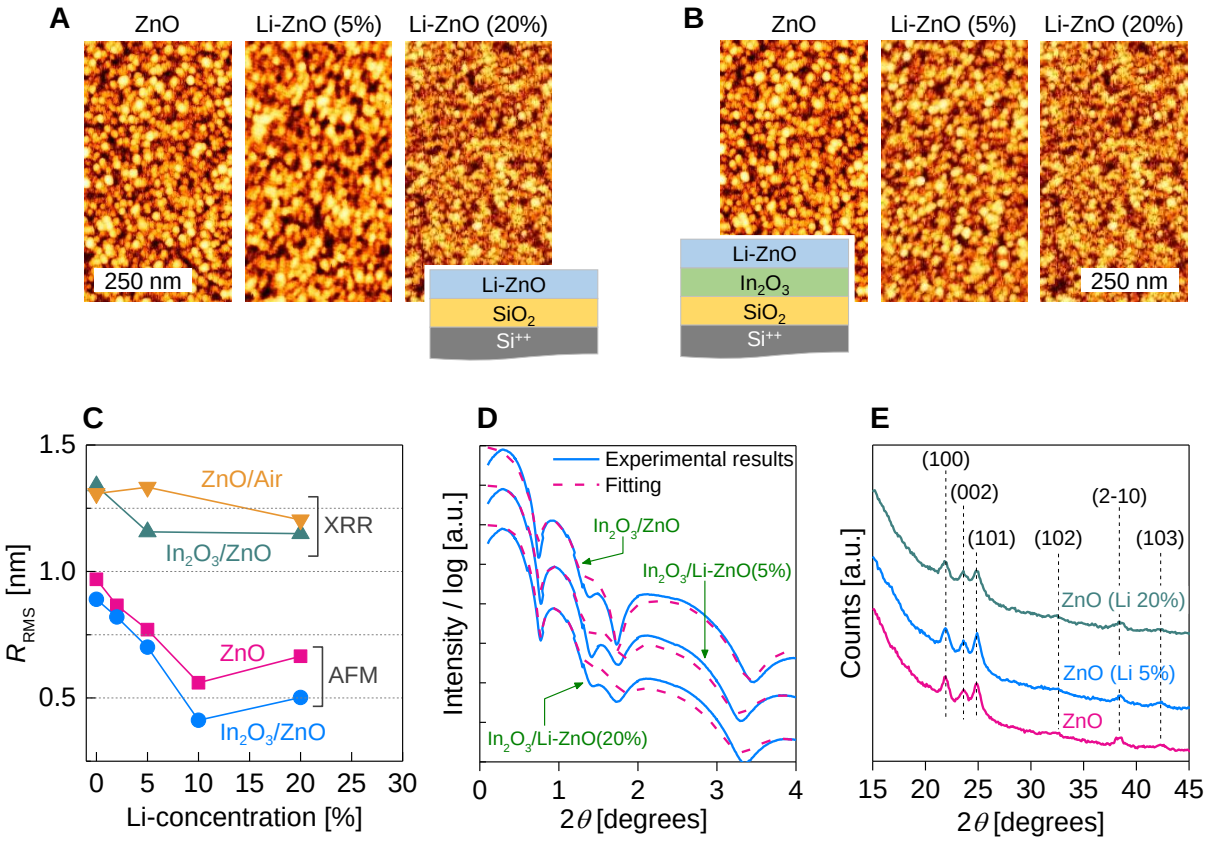


Figure 2. (a) Atomic force microscopy (AFM) surface topography images of pristine ZnO and Li-ZnO layers grown on SiO_2 (inset). (b) AFM surface topography images of pristine In_2O_3/ZnO and In_2O_3/Li-ZnO heterojunctions (inset). (c) Evolution of RMS surface/interface roughness (R_{RMS}) in single layer ZnO and In_2O_3/ZnO heterojunctions for different Li concentrations acquired from x-ray reflectivity (XRR) and AFM measurements. (d) XRR patterns of In_2O_3/Li-ZnO heterojunctions where the Li concentration varies from 0 to 20%. (e) Grazing incident x-ray diffraction patterns measured for ZnO layers with 0%, 5% and 20% Li concentration.

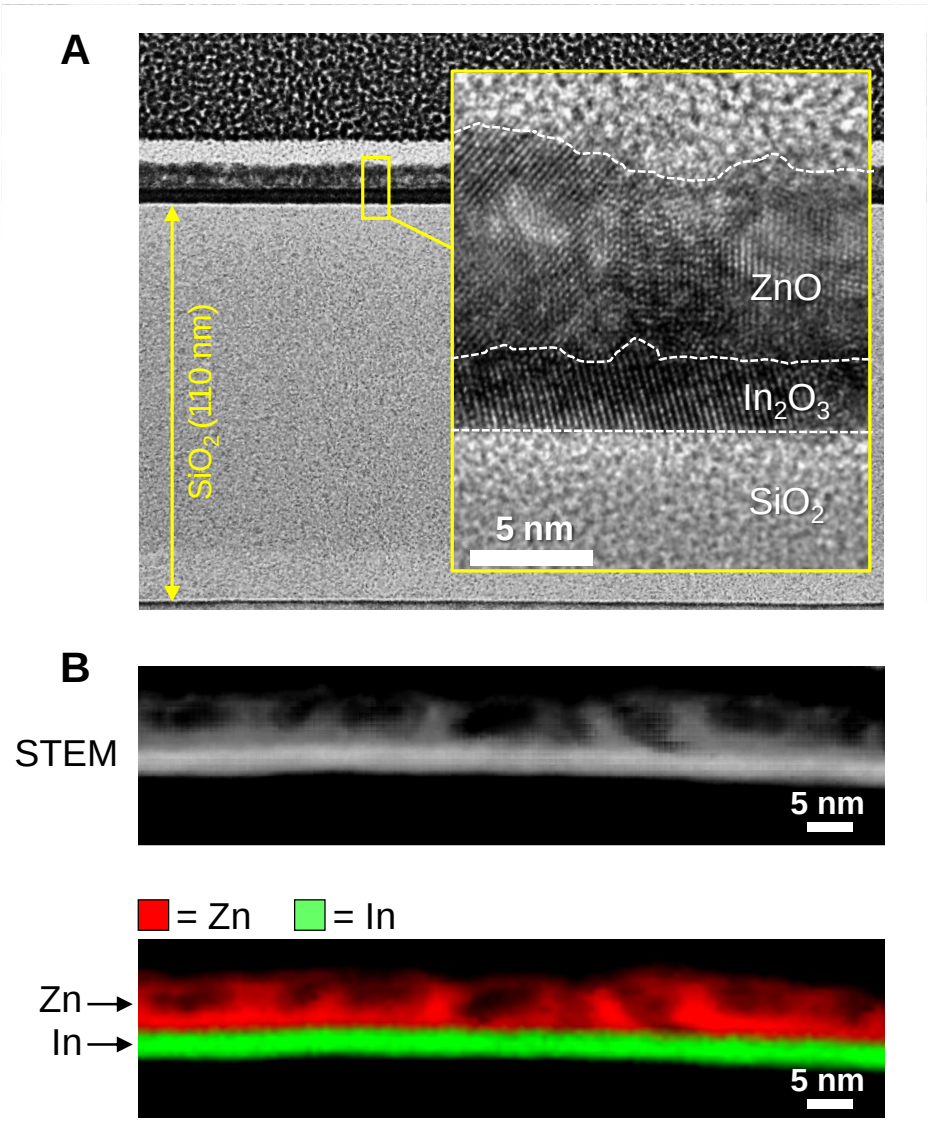


Figure 3. (a) High-resolution transmission electron microscope (HETEM) cross-section images of SiO_2/In_2O_3/Li-ZnO heterojunctions. (b) Scanning transmission electron microscopy (STEM) of In_2O_3/ZnO heterojunction and electron energy loss spectroscopy (EELS) mapping of In (Green) and Zn (Red).

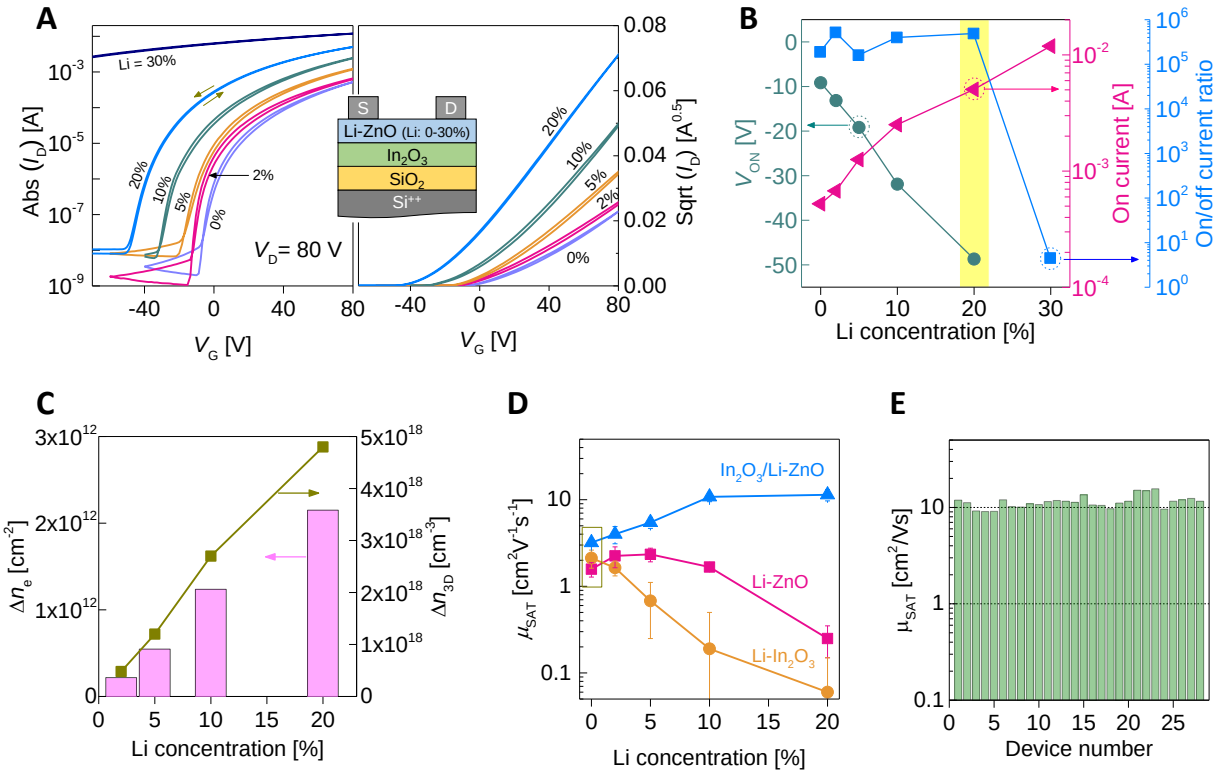


Figure 4. (a) Transfer characteristics and corresponding linear fit from In_2O_3/ZnO heterojunction transistors with different Li-doping ratios of ZnO. (Inset: TG/BC configuration). (b) Evolution of V_{on}, on-current level, and on/off ratio of In_2O_3/Li-doped ZnO heterojunction transistors by varying Li-doping ratios. (c) Evolution of calculated charge densities in channel of In_2O_3/Li-doped ZnO bilayer transistors with different Li doping ratios. (d) Evolution of mobilities of In_2O_3, ZnO, heterojunction transistors under various Li-doping ratios. (e) Histogram plot of mobilities calculated by In_2O_3/Li (20%)-doped 28 devices from 3 different batches fabricated in parallel.

Table 1. Key device parameters of BG-TC In_2O_3/Li-ZnO heterojunction TFTs. Values of μ_{SAT} were evaluated in the saturation region at V_D = 80 V using the gradual approximation. The channel width and length of all transistors analysed were 1 mm and 100 µm, respectively.

Channel Layer	μ_{SAT}* [cm^2/Vs]	On/Off ratio	V_{TH} [V]	V_{ON} [V]	Δn [10^{11} cm^{-2}]	Δn_{3D}† [10^{18} cm^{-3}]
In_2O_3/ZnO (0%)	3.2 (±0.3)	1.9×10^5	12.5 (±2.0)	-9.16	N/A	N/A
In_2O_3/Li-ZnO (2%)	4.0 (±0.3)	5.2×10^5	5.9 (±1.3)	-13.16	2.16	0.73
In_2O_3/Li-ZnO (5%)	5.47 (±0.8)	1.6×10^5	4.0 (±1.0)	-19.2	5.46	1.82
In_2O_3/Li-ZnO (10%)	10.8 (±1.6)	4.0×10^5	2.3 (±0.9)	-31.9	12.4	4.12
In_2O_3/Li-ZnO (20%)	11.4 (±1.7)	4.5×10^5	2.12 (±1.1)	-48.7	21.6	7.2

*Mobility values represent averages calculated from at least 10 devices.

† The volume of the channel by assuming an average of 4.5 nm as In_2O_3 and interface of heterojunction.

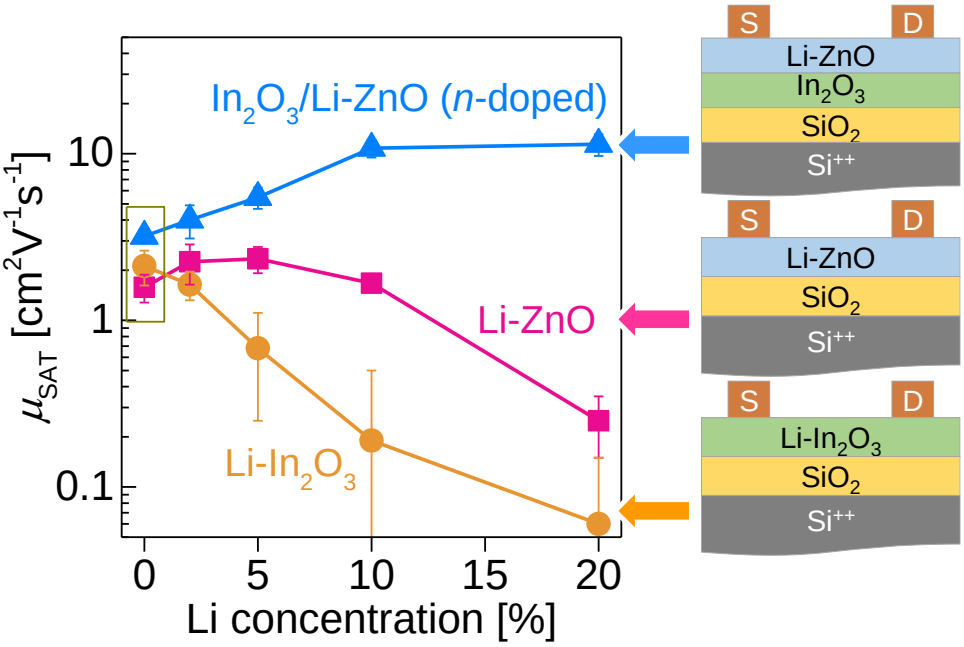
Modulation doping of isotype In_2O_3/ZnO heterojunction transistors fabricated from solution is demonstrated. Selective *n*-type doping of the top ZnO layer with Li is used to improve the electron mobility and operating stability of In_2O_3/ZnO heterojunction transistors, while maintaining the processes temperature at ≤200 °C. The method is simple and potentially applicable to other material systems.

Keywords: Metal oxides; semiconductors; thin film transistors; modulation doping; heterojunction transistor; solution processing; electron mobility.

Dongyoon Khim, Yen-Hung Lin, Sungho Nam, Hendrik Faber, Kornelius Tetzner, Ruipeng Li, Qiang Zhang, Jun Li, Xixiang Zhang, Thomas D. Anthopoulos**

Modulation-Doped In_2O_3/ZnO Heterojunction Transistors processed from Solution

ToC Figure



Supporting Information

Modulation-Doped In_2O_3/ZnO Heterojunction Transistors processed from Solution

Dongyoon Khim, Yen-Hung Lin, Sungho Nam, Hendrik Faber, Kornelius Tetzner, Ruipeng Li, Qiang Zhang, Jun Li, Xixiang Zhang, Thomas D. Anthopoulos**

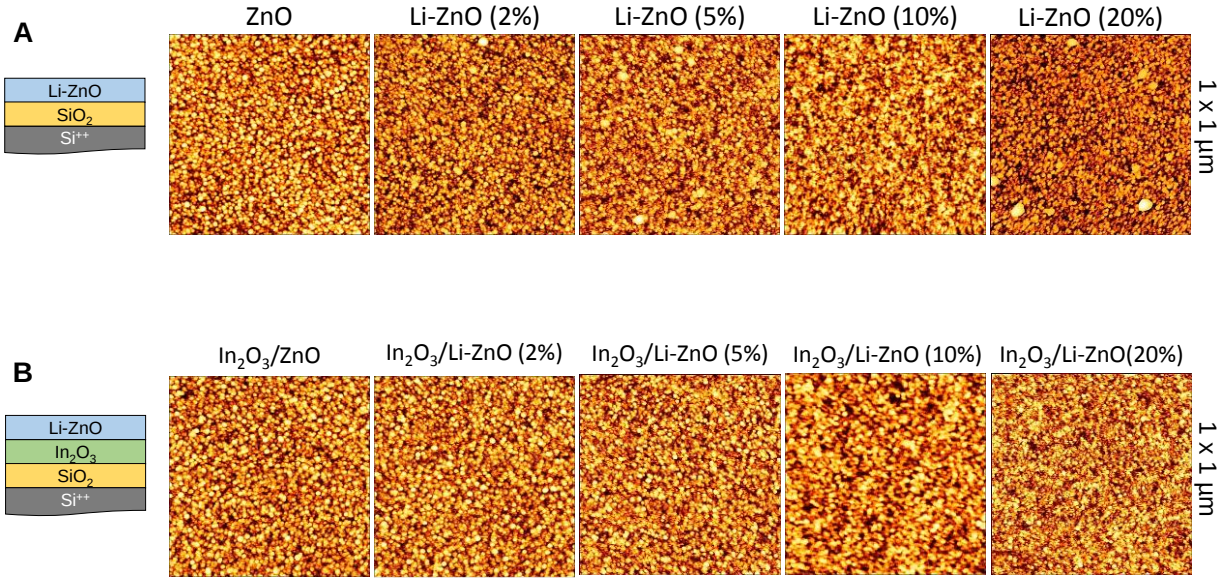


Figure S1. Atomic force microscopy (AFM) images of the surface topographies of: (a) pristine and Li-doped ZnO layers spin-cast on SiO_2, and (b) pristine and Li-doped ZnO-based In_2O_3/SiO_2 heterojunctions.

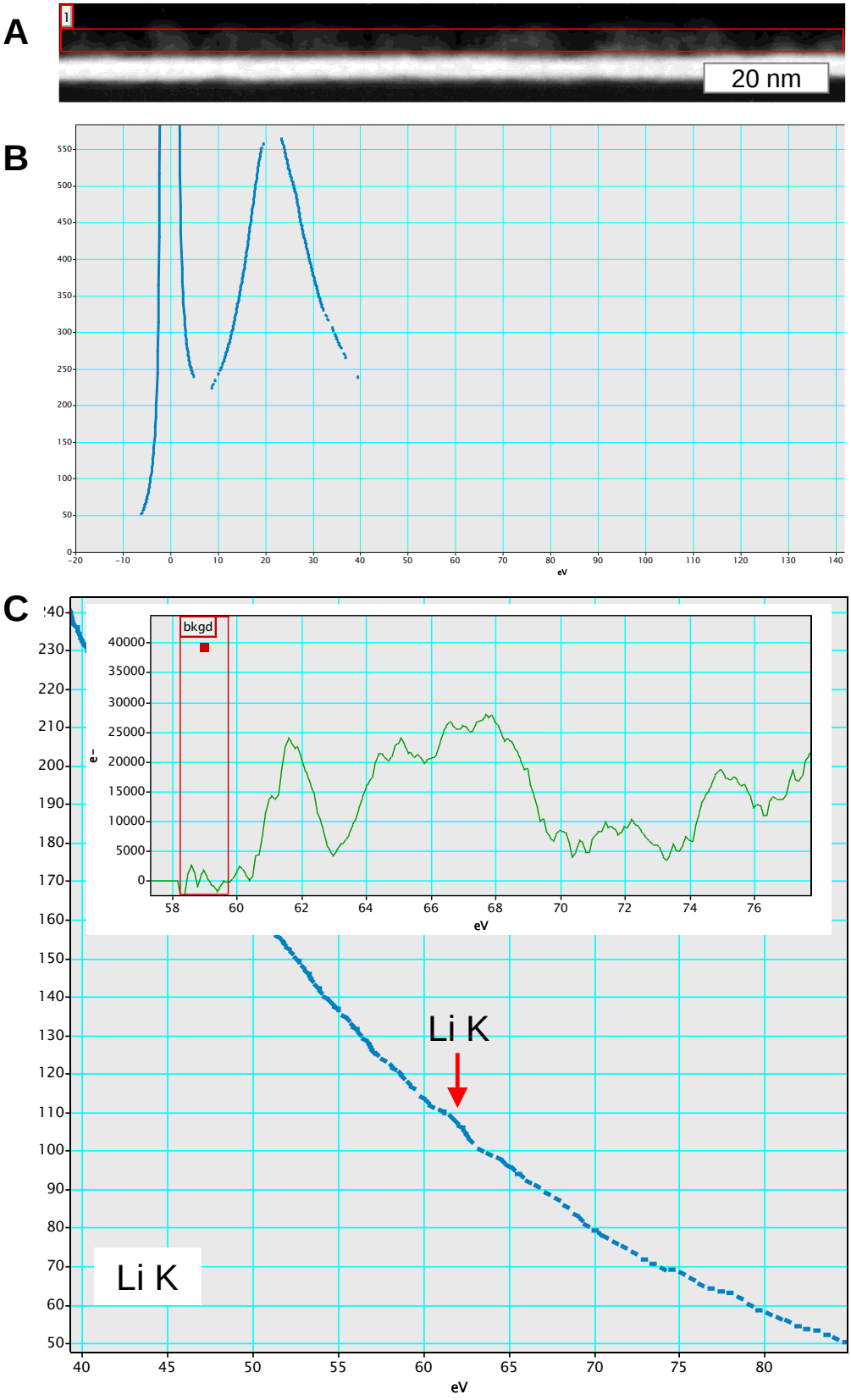


Figure S2. (a) Scanning transmission electron microscopy (STEM) image of the In_2O_3/Li-ZnO(20%) heterojunction. The red rectangle highlights the Li-ZnO(20%) region where electron energy loss spectroscopy (EELS) was performed. (b) EELS spectrum obtained from the Li-ZnO(20%) region, with (c) showing a zoomed in part of the spectrum revealing possible signature of the Li-K edge.

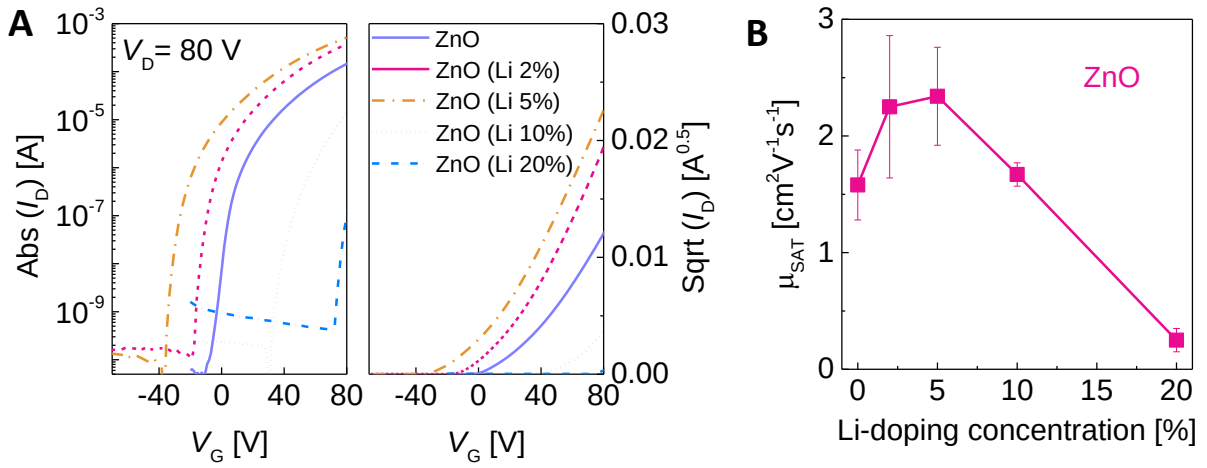


Figure S3. (a) Transfer characteristics and corresponding $I_D^{0.5}$ vs. V_G plots obtained for pristine and Li-doped single layer ZnO BG-TC TFTs. (b) Evolution of mobility with Li concentration for ZnO TFTs.

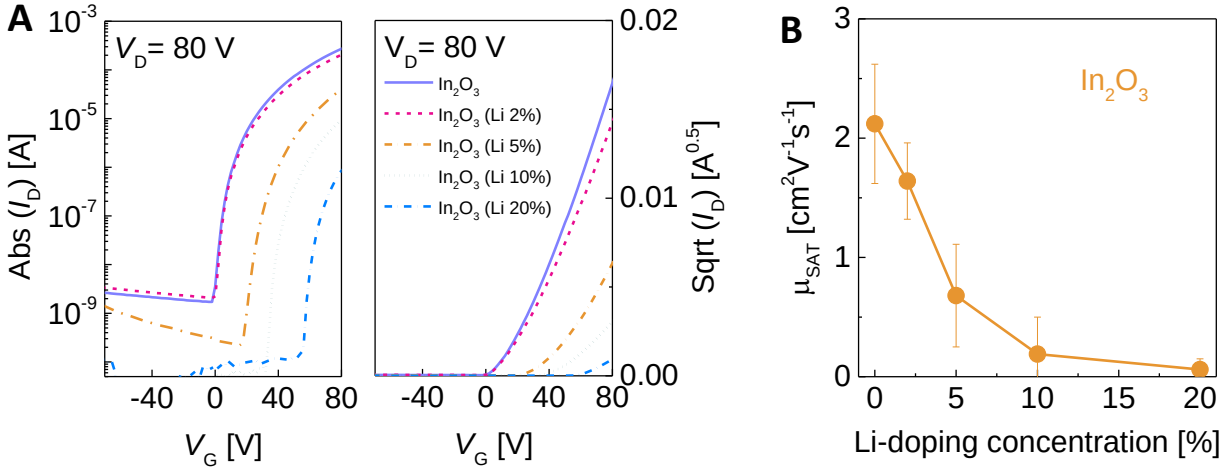


Figure S4. (a) Transfer characteristics and corresponding $I_D^{0.5}$ vs. V_G plots obtained for pristine and Li-doped single layer In_2O_3 BG-TC TFTs. (b) Evolution of electron mobility with Li concentration for the In_2O_3 TFTs.

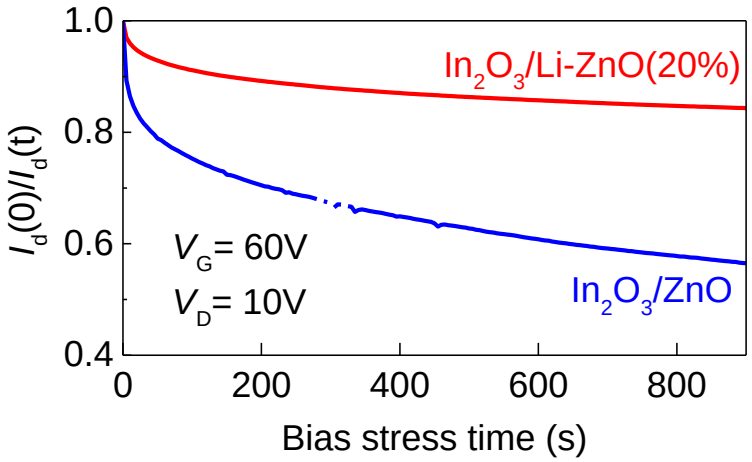


Figure S5. Bias stress characteristics measured for BG-TC transistors based on pristine and Li-ZnO In_2O_3/Li-ZnO heterojunctions. Normalized current under the constant bias stress for In_2O_3/ZnO and In_2O_3/Li-ZnO(20%) TFTs measured at V_G= 60 V and V_D= 10 V.

Table S1. Summary of electrical parameters of BG/TC ZnO TFTs with W/L = 1 mm/100 µm. The electron mobility values were evaluated in the saturation region at V_D = 80 V, using the gradual channel approximation model.

Semiconductor	μ_{SAT}* [cm^2/Vs]	On/Off ratio	V_{TH} [V]	V_{ON} [V]
ZnO (0%)	1.51 (±0.3)	2.4×10^6	28.5	-10
Li-ZnO (2%)	2.25 (±0.61)	3.5×10^6	17.5	-19
Li-ZnO (5%)	2.34 (±0.42)	8.9×10^6	4.98	-36
Li-ZnO (10%)	1.67 (±0.1)	2.2×10^6	67.1	30
Li-ZnO (20%)	0.25 (±0.1)	240	79.0	71

*Mobility values represent averages calculated from at least 10 devices.

Table S2. Summary of electrical parameters of BG/TC In_2O_3 TFTs with W/L = 1 mm/50 µm. The electron mobility values were evaluated in the saturation region at V_D = 80 V using the gradual channel approximation model.

Semiconductor	μ_{SAT}* [cm^2/Vs]	On/Off ratio	V_{TH} [V]	V_{ON} [V]
In_2O_3 (0%)	2.21 (±0.5)	1.5×10^5	19.8	-1.92
Li-In_2O_3 (2%)	1.64 (±0.32)	1.0×10^5	19.6	-0.10
Li-In_2O_3 (5%)	0.68 (±0.43)	1.6×10^5	40.1	16
Li-In_2O_3 (10%)	0.19 (±0.31)	1.1×10^5	47.7	32
Li-In_2O_3 (20%)	0.06 (±0.09)	0.6×10^5	61.5	54

*Mobility values represent averages calculated from at least 10 devices.